Supplementary Information

Negative-charge-anchored separators facilitating lithium-ion conduction to stabilize lithium metal anodes

Yating Hu, Chengjie Wang, Yue Wu, Qing Zhao, Ang Li, Qianqian Zhang, Jingbing Liu, Yuhong Jin,* and Hao Wang**

Key Laboratory for New Functional Materials of Ministry of Education, Faculty of Materials and Manufacturing, Beijing University of Technology, Beijing 100124, P. R. China.

*Correspondence author: zhangqianqian@bjut.edu.cn (Q. Zhang), jinyh@bjut.edu.cn (Y. Jin), haowang@bjut.edu.cn (H. Wang).

Content of Supporting Information

7. The corresponding polarization curves of CPS and NCS in the potentiostatic polarization test
8. The comparison of ionic conductivity and t_{Li^+} between CPS and NCS
9. Cyclic voltammograms for Li/Li cells with the CPS and NCS
10. Theoretical Simulations
11. Charge/discharge voltage profiles and EIS spectra of Li/Li symmetric cells with the NCS and CPS
12. Digital photos, top-view and side-view SEM images of the fresh lithium metal
13. The galvanostatic intermittent titration technique (GITT) curve
14. Cycling performance of LFP/Li batteries equipped with NCS and CPS at 1 C
15. References

1. The fabrication process of the Negative-Charge Separator (NCS)

The Negative-Charge Separator (NCS) was prepared using the typical nonsolvent-induced phase separation (NIPS) method. As illustrated in Fig. S1, here the solvent used was N, N dimethylformamide, and four different thicknesses of separators were prepared by casting a well-dispersed PVDF slurry onto a smooth glass plate substrate using an automatic blade coater with controlled gap and speed, after which the substrate was immersed in solvent-free deionized water.

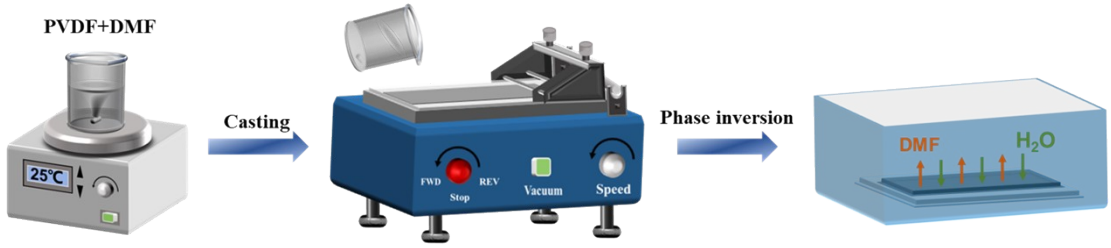

Fig. S1 Schematic illustration for the fabrication process of the Negative-Charge Separator (NCS).

2. Cross-sectional SEM images of the NCS of other thicknesses

From the cross-sectional image of the NCS (Fig. S2), it could be measured that the thicknesses of the prepared separators were 35 μm, 50 μm and 78 μm, except for the NCS with a thickness of 65 μm.

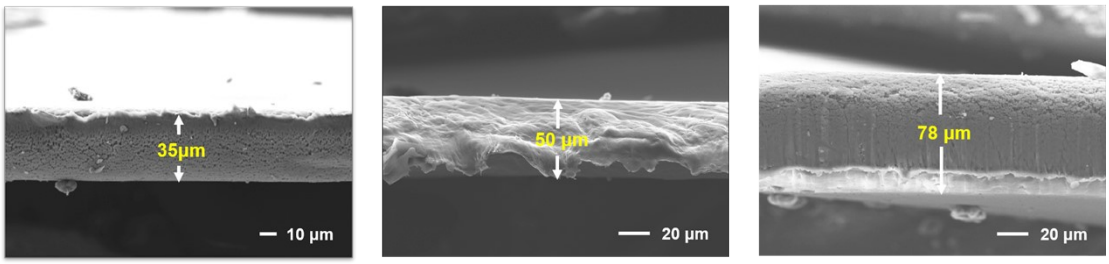

Fig. S2 Cross-sectional SEM images of the NCS of other thicknesses.

3. FTIR spectra and XRD patterns of the β-PVDF

A Fourier transform infrared (FTIR) spectrum was measured to confirm the component of the NCS separator. As shown in Fig. S3, the peaks at 1402 and 3023 cm^{-1} respectively corresponded to the bending and stretching vibrations of CH_2 in the alkyl chain, and the vibrations bands at 1070, 1178 cm^{-1} can be attributed to symmetrically stretched -CF_2[1].

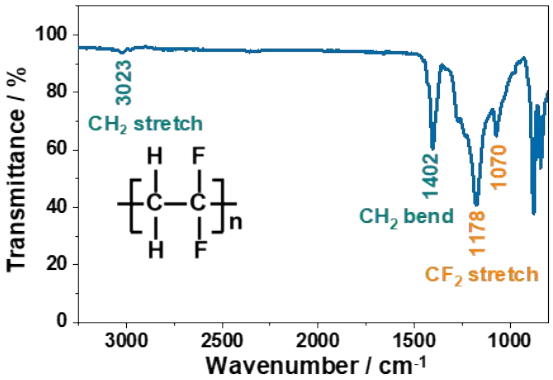

Fig. S3 FT-IR spectra of the NCS.

When polyvinylidene fluoride (PVDF) was fabricated into films, this semi-crystalline polymer can crystallize into different chain-like structures. Common crystalline forms include α and β crystalline forms. α -PVDF was non-polar, with two polymer chains per α phase and the dipole of each of the two polymer chains facing in a different direction. β-PVDF had all-trans conformations, with the F and H atoms located on opposite sides of the polymer backbone, making it the most polar form[2]. The crystalline phase of PVDF in the NCS was characterized by Fourier Transform Infrared (FTIR) spectroscopy. The principle of FTIR measurements was the perceived change

in the orientation of the CF_2 bond in the PVDF molecule, showing strong characteristic FTIR peaks at 840 cm^{-1} (CH_2 rocking) and 510 cm^{-1} (CF_2 bending) as shown in Fig. S4a[3,4]. X-ray diffraction (XRD) could also characterize the crystalline phase of PVDF in the NCS. The XRD diffraction angle $2\theta = 20.6°$ measured in Fig. S4b, both of which demonstrated that the prepared separator was a β-phase dominated PVDF (β-PVDF).

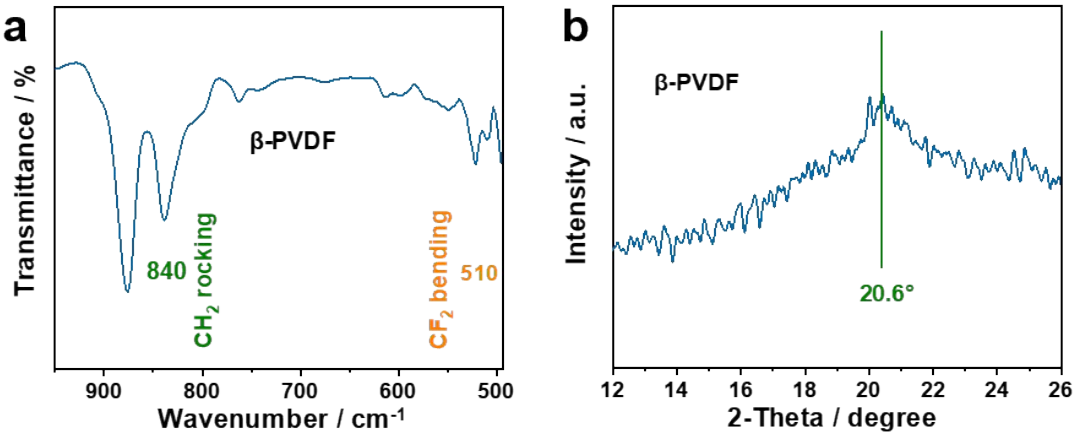

Fig. S4 (a) FTIR spectra and (b) XRD patterns of the β-PVDF.

4. The porosity, electrolyte uptake, and contact angle of the CPS and NCS

The porosity corresponding to the CPS and the prepared separators (35 µm, 50 µm, 65 µm, 78 µm) were 45%, 76%, 78.33%, 81.67% and 78.67% respectively. The electrolyte uptake corresponding to the CPS and the prepared separators (35 µm, 50 µm, 65 µm, 78 µm) were 84.33%, 319.50%, 324.67%, 329.67% and 323.33% respectively (Fig. S5a). As illustrated in Figure S5b, the contact angle of the electrolyte on the surface of the prepared separators (35 µm, 50 µm, 65 µm, 78 µm) were 34.33°, 31.15°, 24.62° and 27.34° respectively, while the contact angle of CPS was 40.54°. The porosity, electrolyte uptake and electrolyte wettability of the prepared separators were much better than those of the CPS.

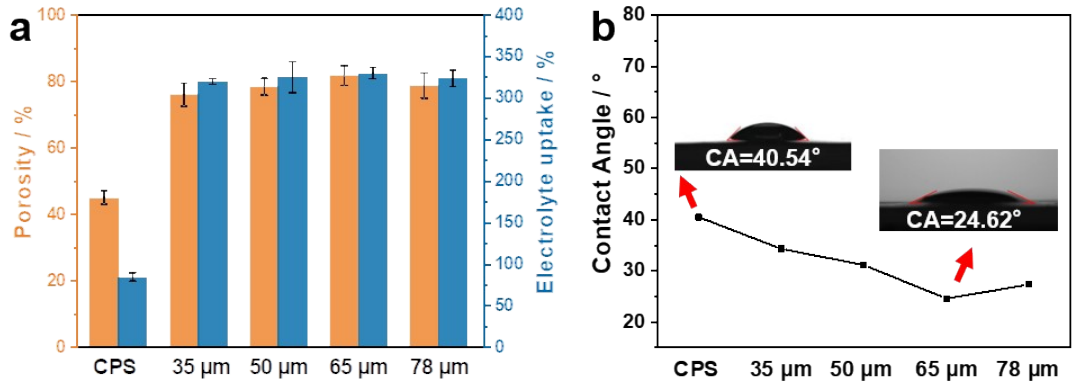

Fig. S5 The porosity, electrolyte uptake (a), and contact angle (b) of the CPS and NCS.

5. LSV curves of asymmetric Li/CPS/SS and Li/NCS/SS cells

As shown in Fig. S6, an anode peak appeared at 4.4 V in the CPS based cell owing to the deposition of carbonate solvent in the electrolyte. In terms of the NCS, the electrolyte decomposition voltage reached up to 5.1 V, indicating a higher security enabled in LMBs.

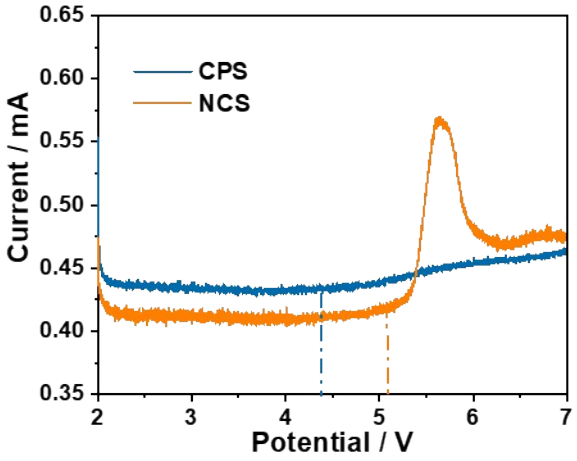

Fig. S6 LSV curves of asymmetric Li/CPS/SS and Li/NCS/SS cells.

6. Thermal stability of different separators

The two separators were further exposed at various temperatures for 30 min to study the thermal stability in a visual mode. As shown in Fig. S7, it could be found that CPS shrunk under 120 ^{o}C and melted into a stripe state when the temperature was evaluated to 180 ^{o}C. However, the NCS could maintain no heat shrinkage deformation up to 140 ^{o}C. This indicated that the NCS had a superior thermal dimensional stability compared with the CPS one.

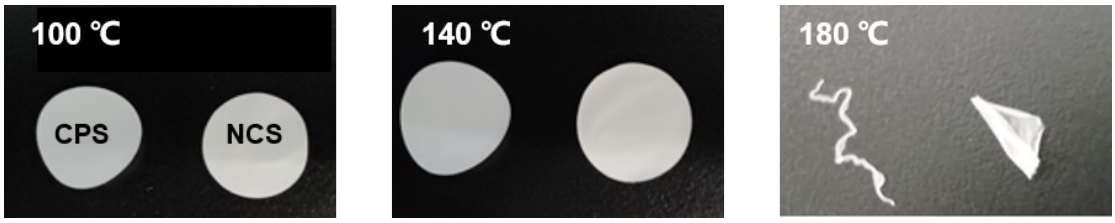

Fig. S7 Photographs of the CPS and NCS at different heat temperatures.

TGA curves of CPS and NCS were presented in Fig. S8. The thermal decomposition of the CPS and the NCS were tested by thermogravimetry analysis (TGA). All the samples were sintered from 25 to 1000 ^{o}C at a rate of 5 ^{o}C min^{-1}. The TGA curve of the NCS showed a weight loss at 400 ^{o}C, whereas the CPS started to decompose at 330 ^{o}C. This indicated that the NCS had a high thermal decomposition temperature compared with the CPS one.

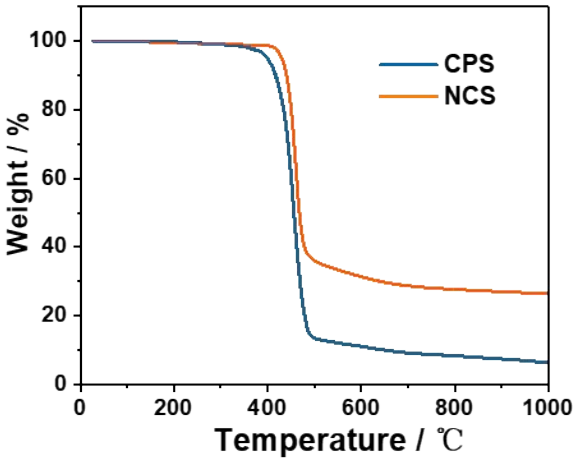

Fig. S8. TG curves of the CPS and NCS.

7. The corresponding polarization curves of CPS and NCS in the potentiostatic polarization test

As shown in Fig. S9, the potentiostatic polarization measurements were carried out from the initial state to the steady state. Initial current (I_0) and steady-state current (I_{ss}) were recorded during potentiostatic polarization with voltage bias of 10 mV.

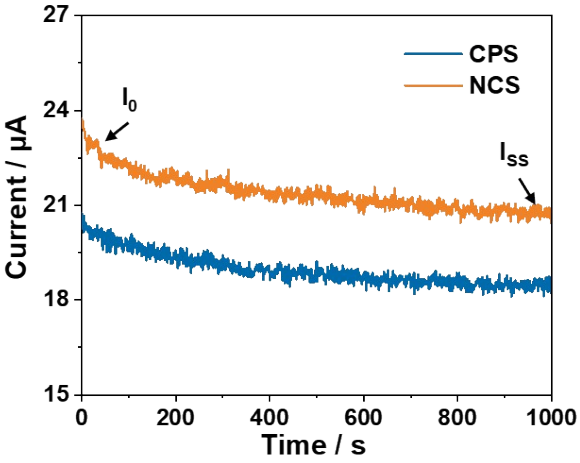

Fig. S9 The corresponding polarization curves of CPS and NCS in the potentiostatic polarization test.

8. The comparison of ionic conductivity and t_{Li}^+ between CPS and NCS

As shown in Fig. S10, the values of t_{Li}^+ and σ first increased and then decreased with the increase of separator thickness because the ion transport was blocked by the excessively thick separator with a high membrane resistance.

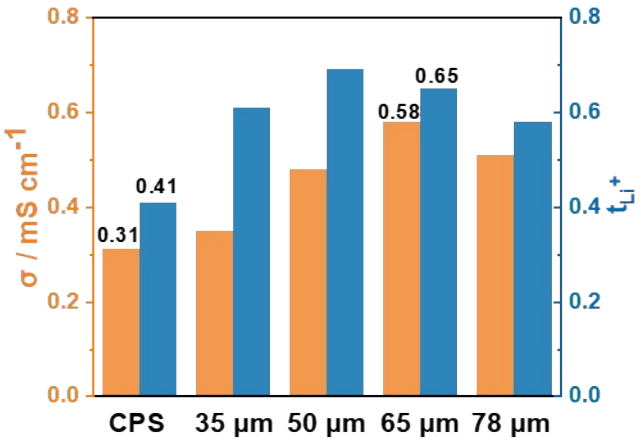

Fig. S10 The comparison of ionic conductivity and t_{Li}^+ between CPS and NCS.

9. Cyclic voltammograms for Li/Li cells with the CPS and NCS

The exchange current density (i_0) was measured by linearly fitting the Tafel plots at a sweep rate of 0.1 mV s^{-1} from -100 to 100 mV. Cyclic voltammograms for Li/Li cells with the NCS and CPS showed that the cells with the NCS show a steeper slope.

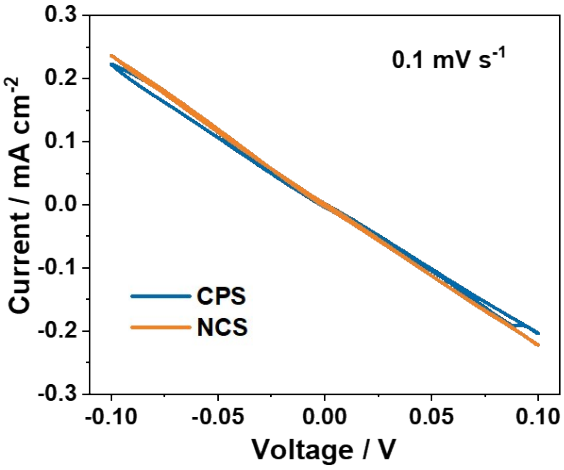

Fig. S11 Cyclic voltammograms for Li/Li cells with the CPS and NCS.

10. Theoretical Simulations

The theoretical simulations were carried out based on Poisson and Nernst-Planck (PNP) equations as follows[5,6]:

$$j_i = D(\nabla c_i + \frac{Z_i F C_i}{RT} \nabla \varphi) \quad \text{(S1)}$$

$$\nabla^2 \varphi = -\frac{F}{\varepsilon} \sum Z_i C_i \quad \text{(S2)}$$

$$\nabla \cdot j_i = 0 \quad \text{(S3)}$$

Where j_i, D, c_i, φ, and ε were ionic flux, diffusion coefficient, ion concentration, electrical potential, and the dielectric constant of the electrolyte solution respectively. *F* was Faraday's constant. *R* was the universal gas constant. *T* was the absolute temperature, respectively. Equation (S1) was the flux equation (Nernst-Planck equation). Equation (S2) was the Poisson equation, which described the relationship between potential and ion concentration. When the system reached a stationary regime, the flux shall satisfy the time-independent continuity equation (S3). The coupled equations (S1) to (S3) could be solved under appropriate boundary conditions. The ion transport channel was simplified as the 2D model. The simulation model was shown in Fig. S12, it contained a 2000 nm long, 60 nm pore size nano-channel. Two electrolyte reservoirs were introduced to decrease the effect of entrance/exit mass transfer resistances on the overall ionic transport. The electrolyte solution chosen was 0.1 mM KCl aqueous solution, PVDF powder was first dissolved in methanol solution, a small amount of the mixture was drawn into KCl aqueous solution and the final measured ζ potential value was -25.5 mV. The electrolyte in the two reservoirs was experimentally set to 0.1 mM KCl aqueous solution, which corresponded to a Debye length (i.e. double

layer thickness) of 30.5. We set the surface charge density as 0.592 mC m^{-2} to acquire the relevant concentration profile.

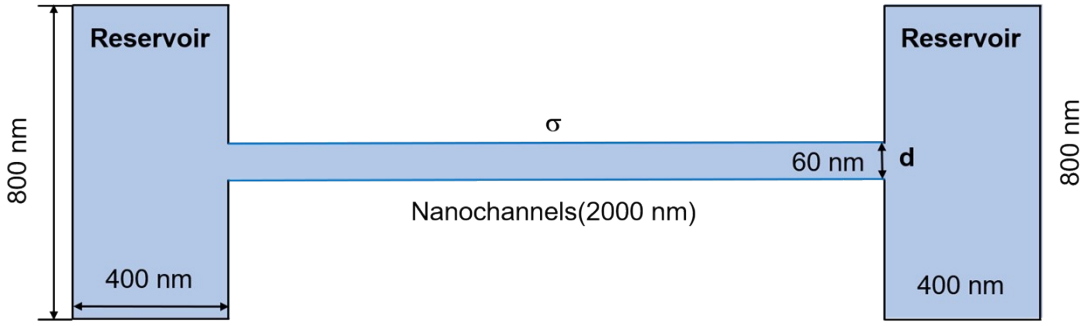

Fig. S12 A numerical simulation model based on PNP theory. The model was not drawn on a real scale.

In the NCS model, the cation concentration was much higher than that of the anion, indicating a cation-selective behavior (Fig. S13). Compared with the CPS model, cations in the NCS demonstrated higher concentration and wider distribution range at an applied bias (0 V) (Fig. S14), which was attributed to that the negatively charged C-F groups in NCS enhanced space charge density.

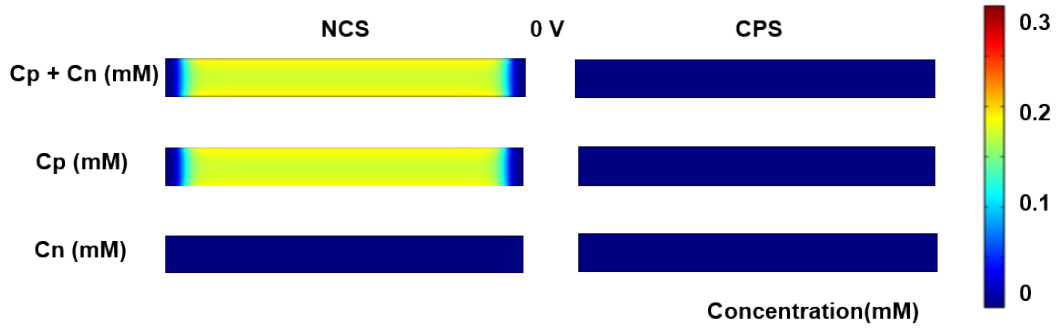

Fig. S13 The calculated cation and anion concentration profiles based on the NCS and CPS models at an applied bias (0 V).

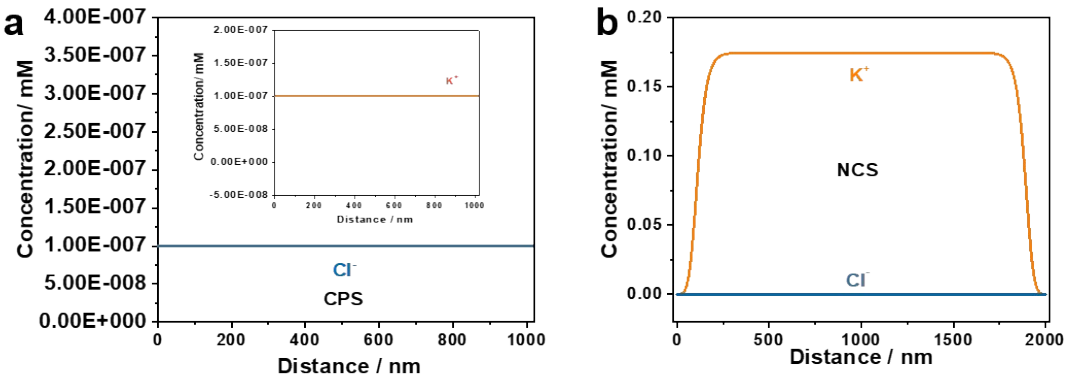

Fig. S14 The K^+ and Cl^- concentration profiles of the CPS and NCS under 0 V.

11. Charge/discharge voltage profiles and EIS spectra of Li/Li symmetric cells with the NCS and CPS

(1) When the current density was 1 mA cm^{-2} with the areal capacity of 0.5 mAh cm^{-2}, the Li/NCS/Li symmetric cell exhibited long-term cycle stability with smooth and stable polarization voltages over 1500 cycles. The detailed voltage profiles from the 1495th to the 1500th cycle corresponding to Fig. S15 were shown in Fig S15 Inset, which showed that the overpotential of Li/NCS/Li cell was stably maintained at a low value. By contrast, the polarization of the CPS increased sharply after 100 h and fluctuated markedly after 150 h due to the uncontrollable formation of Li dendrite and "dead" Li on the surface of the Li metal anode. This problem was particularly prominent at higher current densities.

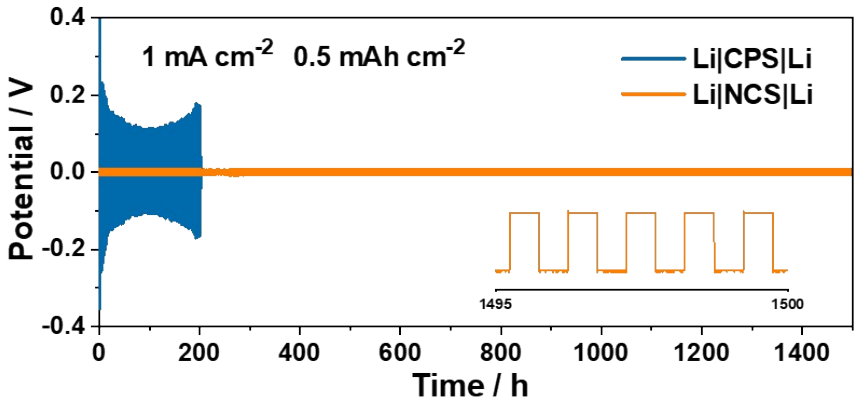

Fig. S15 Charge/discharge voltage profiles of Li/Li symmetric cells with the NCS and CPS at a current density of 1 mA cm^{-2} with areal capacity of 0.5 mAh cm^{-2}. Inset showed the cycling of the NCS-based cell during 1495 to 1500 h.

(2) As shown in Fig. S16, the Li/CPS/Li cell interface became unstable after 20 hours at a current density of 3 mA cm^{-2} (area capacity of 1.5 mAh cm^{-2}), while Li/NCS/Li

could cycle stably for 150 hours. The detailed voltage profiles from the 145th cycle to the 150th cycle was shown in the inset of Fig. S16, which indicated a low and smooth polarization voltage for Li/NCS/Li.

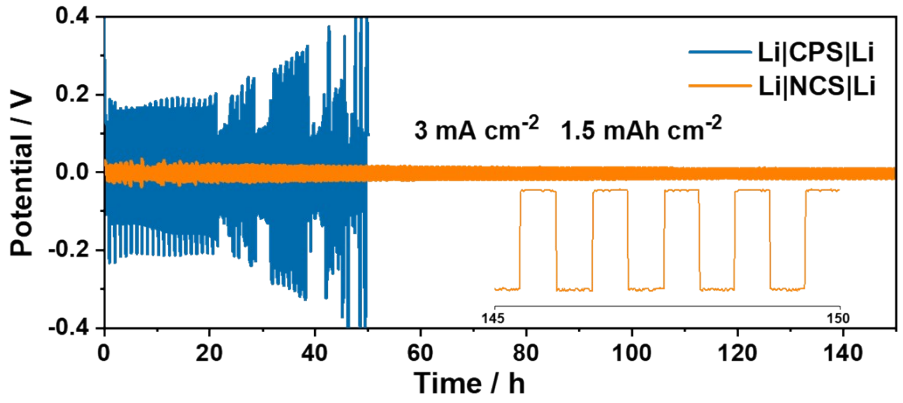

Fig. S16 Voltage curves corresponding to long-cycle tests using Li/Li symmetric cells with NCS and CPS at a current density of 3 mA cm^{-2}. Inset showed the detailed voltage profile of the NCS-based cell during 145th to 150th.

(3)

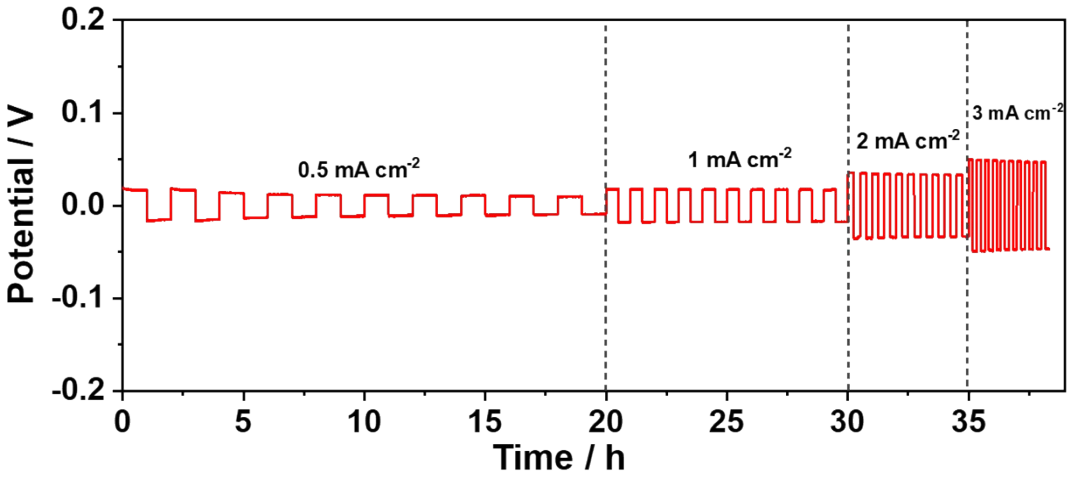

Fig. S17 Cell voltage evolution with time for Li/Li symmetric cells with NCS at current densities from 0.5 to 3 mA cm^{-2} and at an area capacity of 0.5 mAh cm^{-2}.

(4) The local magnification of the EIS spectrum showed more clearly the change in

charge transfer resistance after several cycles.

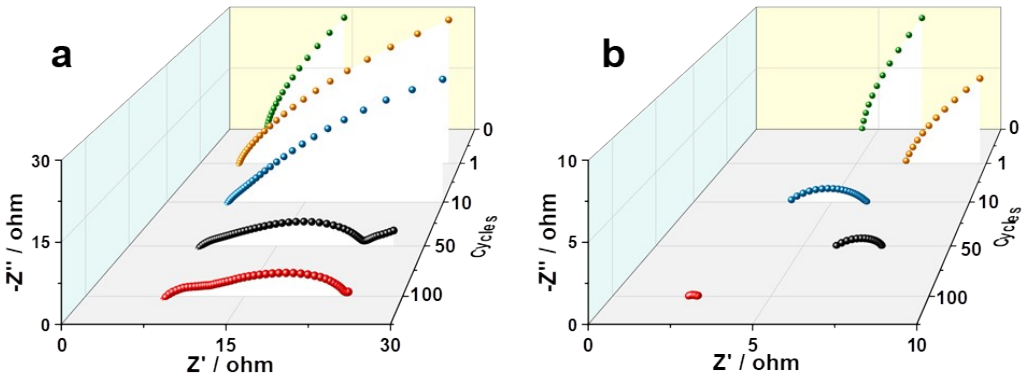

Fig. S18 Local magnification of the EIS spectrum of a symmetrical lithium battery with CPS (a) and NCS (b) in the initial state and after cycling at 1 mA cm^{-2} (0.5 mAh cm^{-2}) for 0, 1, 10, 50 and 100 hours.

12. Digital photos, top-view and side-view SEM images of the fresh lithium metal

As shown in Fig. S19, the fresh Li metal anodes presented a dense, smooth, and defect-free surface.

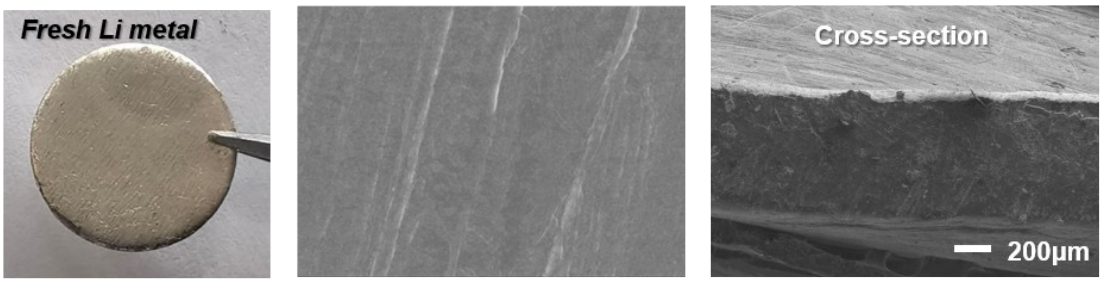

Fig. S19 Digital photos, top-view and side-view SEM images of the fresh lithium metal.

13. The galvanostatic intermittent titration technique (GITT) curve

The electrochemical properties of the cathode material are mainly influenced by the kinetics of Li^+ insertion/extraction, so we measured the chemical diffusion coefficients of Li ions (D_{Li}^+) during repeated cycles using the galvanostatic intermittent titration technique (GITT)[7]. The GITT curve showed the evolution of the quasi-equilibrium voltage under repeated charge/discharge and resting conditions. It could be seen that the charge/discharge time of the NCS-equipped cell was longer than that of the CPS-equipped cell, and thus the discharge capacity of the LFP/NCS/Li cell was significantly enhanced (Fig. S20a and b).

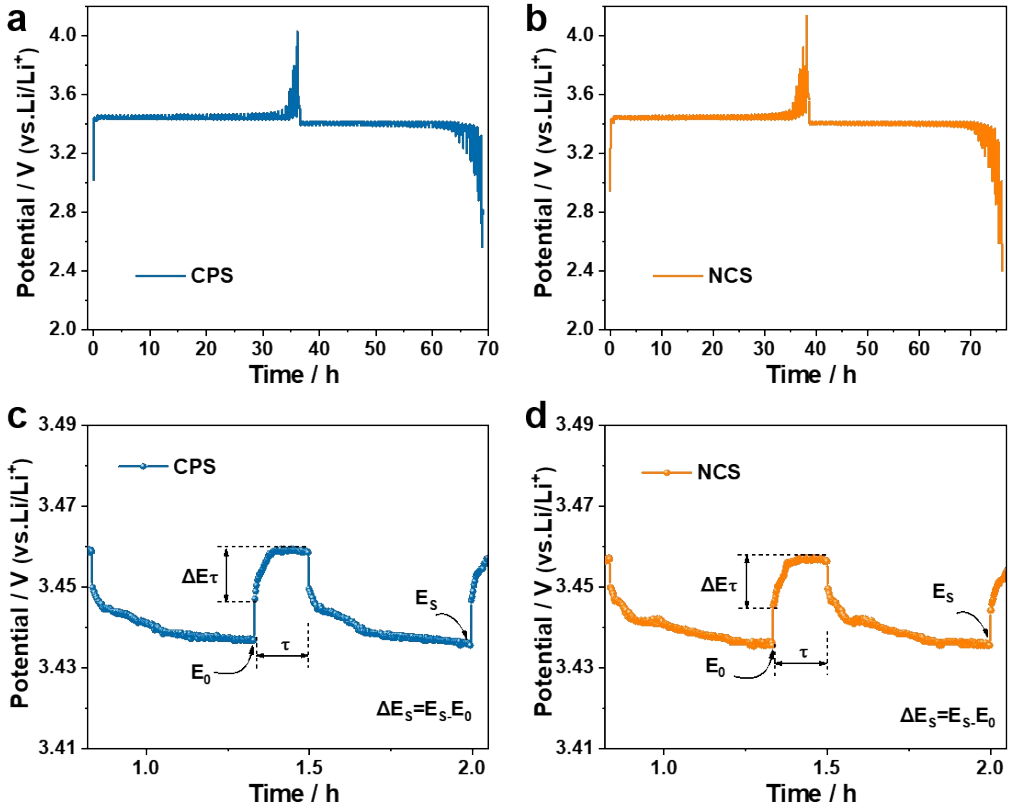

Fig. S20 GITT measurements of LFP/Li cells equipped with CPS (a) and NCS (b). Current step diagrams at plateau of the second lithiation process: (c) CPS; (d) NCS.

The D_{Li}^+ was calculated based on the following equation (S4) (assuming that the battery potential is linearly proportional to $\Delta\tau^{1/2}$)[8]:

$$D = \frac{4}{\pi \Delta \tau} \left(\frac{m_B V_M}{M_B S} \right)^2 \left(\frac{\Delta E_S}{\Delta E \tau} \right)^2 \quad \text{(S4)}$$

where S is the geometric area of the electrode, m_B, M_B, and V_M are the mass, molar mass and molar volume of the electrode active material, respectively, while definitions for other parameters in the above equation, including $\Delta\tau$, $\Delta E\tau$, ΔE_S, were displayed in Fig.S20c and d). The Li^+ diffusion coefficients of 2.78×10^{-11} cm^2 s^{-1} and 2.90×10^{-11} cm^2 s^{-1} for the CPS-equipped and NCS-equipped cells, respectively, further confirmed the fast ion transport behavior of the NCS-equipped cell.

14. Cycling performance of LFP/Li batteries equipped with NCS and CPS at 1 C

As shown in Figure S21, the cycle performance of the battery was tested at low current density (1 C). The LMBs equipped with the NCS presented superior cyclic stability than that of the CPS one. After 100 cycles under 1 C, LFP/NCS/Li cells could deliver a 95.5% capacity retention. In comparison, LFP/CPS/Li cells had capacity retention of 94.0%.

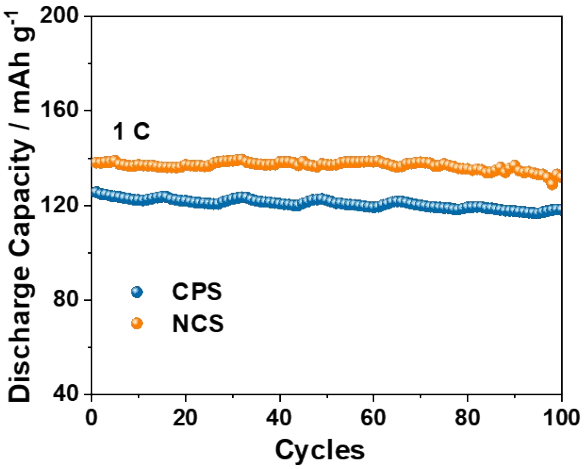

Fig. S21 Cycling performance of LFP/Li batteries equipped with NCS and CPS at 1 C.

15. References

1 Y. Hou, Z. Huang, Z. Chen, X. Li, A. Chen, P. Li, Y. Wang and C. Zhi, *Nano Energy*, 2022, **97**, 107204.

2 A. C. Lopes, P. Martins and S. Lanceros-Mendez, *Prog. Surf. Sci.*, 2014, **89**, 239-277.

3 J. S. Andrew and D. R. Clarke, *Langmuir*, 2008, **24**, 670-672.

4 S. Ramasundaram, S. Yoon, K. J. Kim and J. S. Lee, *Macromol. Chem. Phys.*, 2008, **209**, 2516-2526.

5 C. Cheng, G. Jiang, G. P. Simon, J. Z. Liu and D. Li, *Nat. Nanotechnol.*, 2018, **13**, 685-690.

6 H. S. White and A. Bund, *Langmuir*, 2008, **24**, 2212-2218.

7 H. Li, L. Peng, D. Wu, J. Wu, Y.-J. Zhu and X. Hu, *Adv. Energy Mater.*, 2019, **9**, 1802930

8 J.-Y. Shih, G.-Y. Lin, Y.-J. J. Li, T.-F. Hung, R. Jose, C. Karuppiah and C.-C. Yang, *Electrochim. Acta*, 2022, **419**, 140356.